Original article

Effects of wing pitch kinematics on both aerodynamic and olfactory functions in an upwind surge

Chengyu Li [iD]

Abstract

Flapping wings of insects serve for both generating aerodynamic forces and enhancing olfactory sensitivities when navigating on the odor-rich planet. Despite the extensive investigations of the aerodynamic function of flapping wings, we have limited understanding of how the flapping wings potentially affect the physiological sensitivities during flight. In this paper, direct numerical simulations were used to investigate a fruit fly model in an upwind surging motion. The wing pitch kinematics were prescribed using a hyperbolic function, which can change the wing pitch profile from a sinusoidal function to a step function by adjusting the "C" factor in the hyperbolic function. Both aerodynamic performance and olfactory detections were quantified at various wing pitch kinematics patterns. The effects of flapping wings on the odor transport were visualized using the Lagrangian approach by uniformly releasing passive odor tracers in upstream. The study revealed that the insect had the potential to achieve higher aerodynamic performance by tailoring wing pitch kinematics, but it could reduce the odor mass flux around the antenna. It was suspected that the natural flyers might sacrifice certain aerodynamic potential to enhance their olfactory sensitivity for surviving purposes. In addition, a trap-and-flick mechanism is proposed here during the supination phase in order to enhance the olfactory sensitivity. Similar to the clip-and-fling mechanism for enhancing the force generation during the pronation phase, the newly proposed trap-and-flick mechanism is also due to the wing-wing interaction in flapping flight. These findings could provide important implications for engineering applications of odor-guided flapping flight.

Introduction

Over the past two decades, studies in understanding insect flight have primarily focused on aerodynamic functions of insect wings,[1–5] which is undoubtedly the primary function of the wings. However, insect wings are evolutionarily remarkable, and they are known to serve multiple roles besides flying. For instance, the induced airflow generated by flapping wings can alter the thickness of velocity boundary layer adjacent to olfactory receptors[6,7] and potentially enhance the olfactory sensitivity in an odor-tracking flight.[8] When insects flap their wings to lift its body in the air, the flapping wings will inevitably perturb surrounding chemosensory signals. Presumably, flapping wing kinematics not only plays a critical role in the aerodynamic performance but also influences flight-related physiological sensation.

The aerodynamic basis of flapping wings relies on the smart wing rotation during both translational and reversal phases. In the translational phases, the insect

wing maintains a high angle of attack and generates a tornado-shaped leading-edge vortex attached on the suction surface.[1] In the reversal phases (i.e. supination and pronation), the wing rotation generates rotational circulation and captures the wake developed in the previous translational stroke.[2] As the wing flaps back and forth, the lift generated by the wing can be almost twofold compared with a static wing in the same flow condition.[9] These unsteady aerodynamic mechanisms revealed from hovering motion also apply to a forward flight. However, unlike hovering flight where lift force is almost evenly generated during both downstroke and upstroke, the majority

Department of Mechanical Engineering, Villanova University, Villanova, PA, USA

Corresponding author:
Chengyu Li, Department of Mechanical Engineering, Villanova University, Villanova, PA 19085, USA.
Email: chengyu.li@villanova.edu

of lift (up to 80%) is produced during the downstroke in a forward flight.[10] When insects fly forward, its body will also perturb surrounding airflow and generate a body wake, and this particularly applies to insects with a wide body shape.[11] As the flapping wings interact with the body wake, the overall lift generated by both body and wings can be enhanced up to 19% compared with the sum of insulated body and wings.[12] This lift enhancement mechanism due to the wing–body interaction has been widely observed in various species including cicada,[12] fruit fly,[13] and humming bird.[14] In addition to these fundamental lift enhancement mechanisms, insects have also developed other sophisticated propulsive mechanisms to survive million years of evolution. For instance, previous studies discovered many aerodynamic features that are essential in enhancing aerodynamic function and flight efficiency, including their surface morphology[3] and smart rotation of the trailing edge.[4] Yet, it still remains unknown that how the flow perturbation produced by flapping wing kinematics affects the flow field around olfactory receptors (i.e. antenna) and the associated physiological sensation in addition to the enhancement of the aerodynamic performance.

Insects are flying for purposes. Many insects rely on their olfactory system for detecting food sources, prey, and mates. They can sense odorant plumes emitting from sources of their interest, and then rely on their highly efficient flapping-wing mechanism to follow odor plumes, and track down odor sources. During an odor-guided navigation, flapping wings not only serve as propulsors for lift generation and steering maneuvers, but also actively draw odor plumes to the antenna, mimicking "sniffing" in mammals, which helps enhance olfactory detection and localization. Loudon and Koehl[7] measured the air flow speed near the olfactory antenna of moths using hot-wire anemometry. Their experimental data indicated that flapping motion can increase the rate of interception of pheromone by the sensory hairs on the antennae by at least an order of magnitude beyond that in still air. In addition, Sane and Jacobson[6] experimentally measured the induced airflow generated by tethered hawk moths. They found the magnitude of induced air flow around olfactory antenna varies linearly with wing flapping frequency. Besides flapping motion, the flight trajectory in an odor-guided navigation also directly impacts its associated aerodynamic and olfactory functions. The odor-tracking process consists of two distinct behaviors: surging upwind and zigzagging crosswind. When an insect intercepts a filament of odor, it has a tendency to surge upwind momentarily, and then fly crosswind when it loses the odor or when another filament is intercepted.[15] For example, van Breugel et al.[16] investigated the plume-tracking behavior of fruit flies in a laminar flow wind tunnel. They collected more than 50,000 flight trajectories of fruit flies using an automated data collection system. Data revealed that

flight dynamics play a critical role for fruit flies to perceive the surrounding olfactory landscape. When a fruit fly encounters an attractive odor plume, it initiates an upwind surge for more than 40 flapping cycles, and the plume loss in surge motion triggers the zigzagging crosswind behavior. The flapping wings and flight trajectory can perturb the physical structure of odor plumes and create temporal fluctuations of the plume. The effects of the fluid environment on odor stimulus dynamics have important consequences for animal behavior.[17]

However, there is a lack of quantitative measurement on the effects of flapping wings and flight trajectory on aerodynamics and olfaction. Besides, it poses challenges for the experimental investigations to measure both aerodynamic and olfactory functions in odor-tracking flights due to the tiny size wing, fast flapping motion, and unpredictable flight trajectory. Instead, computational fluid dynamics (CFD) simulation could work as a nonintrusive alternative to study the effects of wing kinematics on both aerodynamic performance and olfactory sensitivity. Although there are many computational studies on insect flight in literature,[18–21] those previous studies are limited as they only considered the aerodynamic performance without paying attention to the physiological consequence. As an exception, Li et al.[8] studied both aerodynamic and olfactory functions of a fruit fly in forward flight motion using direct numerical simulations. Their simulation results revealed that the flapping wings trap odor plume in downstroke and flick the plumes upward during wing reversal. This observation confirms the important effects of wing pitch kinematics on enhancing the local odor concentration in an odor-tracking flight. Yet, this study only examined a single flapping pattern. Although wing pitch kinematics plays an important role in the formation of leading edge vertex (LEV) and its associated aerodynamic performance and trapping upstream odor plume, the effects of wing pitch kinematics on these functions have not been investigated in detail. So far, we have limited knowledge about the consequence of the flapping kinematics on the flow field around the insect olfactory sensors (i.e. antenna). The purpose of the present study is to evaluate the odor trapping process in an upwind surge. A series of numerical simulations were performed using an in-house immersed-boundary-method-based solver. Detailed analyses of aerodynamic performance and its associated olfactory sensitivities are presented and compared for different wing pitching kinematics patterns.

Methodology

Wing kinematics

Fruit fly is not only a noted model organism for genetic studies, but also widely used for aeronautic

navigation.[22–24] The study adopted an anatomically correct fruit fly (*Drosophila*) model that has been used in previous studies.[8,25] The fruit fly wing is treated as a rigid with an aspect-ratio of 3.19. The wing thickness is 3% of the mean wing chord length. Based on the literature of forward flying fruit flies,[10,26] the wing flapping stroke plane is 20° and the fruit fly body is inclined by 45° with respect to the horizontal plane. The complex wing flapping kinematics of real insects can be modeled as a rigid plate rotating through three Euler angles. In the current study, the flapping motion is prescribed by specifying the time course of three Euler angles: wing stroke angle (ψ), wing deviation angle (ϕ), and wing pitch angle (θ), as defined in Figure 1(a). The prescribed wing stroke angle is given in equation (1) with an amplitude of $A_\psi = 140°$. The wing deviation angle is set as $\phi(t) = 0°$ with respect to the stroke plane. The wing pitch angle is described by a hyperbolic function given in equation (2) with an amplitude of $A_\theta = 60°$. As the C factor approaches 0, the wing pitch motion becomes a sinusoidal function, while it tends towards a step function as C factor reaches ∞. The value of Figure 1(b) shows the time course of three Euler angles of flapping wings with different wing pitch profiles. The equations of wing kinematics (equations (1) and (2)) represent a generic flapping motion and are similar to the equations in Berman and Wang.[27] The amplitude of wing stroke and wing pitch angles adopted here are a reasonable representation of the kinematics of fruit fly wing and they are consistent with the previous study[26]

$$\psi(t) = 0.5 A_\psi \cos(2\pi f t) \tag{1}$$

where $\psi(t)$ is the instantaneous wing stroke angle at time t, A_ψ is the stroke amplitude, and f is the flapping frequency.

$$\theta(t) = \frac{A_\theta}{\tanh(C)} \tanh[C \sin(2\pi f t)] \tag{2}$$

where, $\theta(t)$ is the instantaneous wing pitch angle, A_θ is the pitch amplitude, and C factor is a constant value that can control the hyperbolic function changing from a sinusoidal function ($C \to 0$) to a step function ($C \to \infty$).

Numerical method and simulation setup

The governing equations of airflow for insect flight are the unsteady incompressible viscous Navier–Stokes equations. The non-dimensional form of the governing equations is shown in equation (3), and discretized using the collocated grid arrangement, where the primitive variables (u_i and p) are stored in the cell center. The equations are integrated with time using the fractional step method and a second-order central difference scheme in space is employed. A sharp interface immersed boundary method is adopted for handling the complex moving boundaries involved in flapping motion. The complex immersed wing and body surfaces are represented by unstructured triangular elements, while the flow is computed on the Cartesian grids. The boundary conditions on the immersed boundaries are imposed through a ghost-cell procedure. The current numerical treatment can eliminate the need for the mesh regeneration at each time step, and thus save the computational cost. This in-house flow solver has been successfully applied to study canonical revolving wings,[28–30] flapping propulsion problems,[31–34] and insect flight.[8,12,19] The validations of this solver can be found in the author's previous papers.[19,32,35]

$$\frac{\partial u_i}{\partial x_i} = 0, \quad \frac{\partial u_i}{\partial t} + \frac{\partial (u_i u_j)}{\partial x_j} = -\frac{\partial p}{\partial x_i} + \frac{1}{Re} \frac{\partial}{\partial x_j} \left(\frac{\partial u_i}{\partial x_j} \right) \tag{3}$$

where u_i represents three velocity components in the Cartesian coordinate system, p is the pressure, and Re is the Reynolds number.
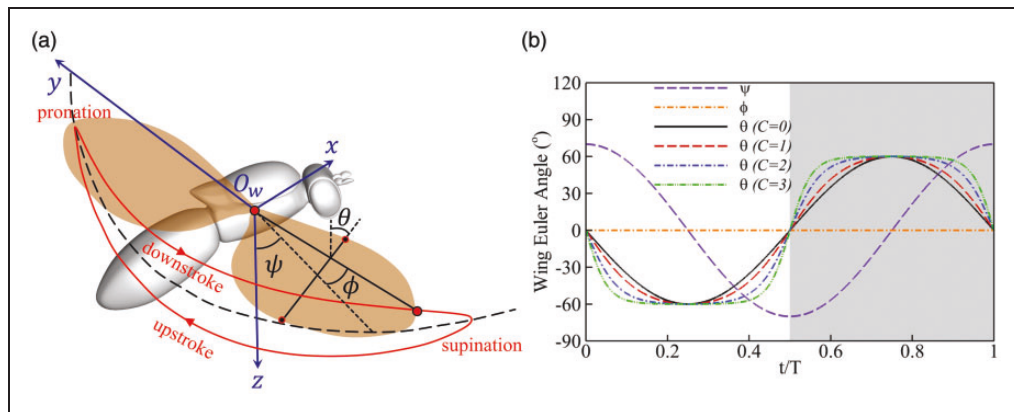

Figure 1. (a) Fruit fly model with the definition of wing Euler angles, wing pitch angle (θ), wing deviation angle (ϕ), and wing stroke angle (ψ). The wing rotates around the pivot points (O_w) within the stroke plane. (b) Time history of wing Euler angles with four different wing pitch patterns by varying C factor. The grey shared region represents the downstroke period.

Figure 2 shows a schematic of the nonuniform Cartesian grid employed in the current study. The computational domain size of the simulation was $49\bar{c} \times 49\bar{c} \times 49\bar{c}$ in terms of mean wing chord length ($\bar{c}$), in order to achieve domain-independent results. The grid size employed in the current simulations was $289 \times 137 \times 249$. The domain mesh had two refined layers. As can be seen in Figure 2, very high resolution was provided in a cuboidal region around the insect body and wings in all three directions with the smallest resolution of $\Delta x = 0.04\bar{c}$. Around this region, there was a secondary denser layer with $\Delta x = 0.09\bar{c}$. Beyond the secondary denser layer, the grid was stretched rapidly. At the upstream boundary, the Dirichlet boundary condition was applied with a constant incoming flow velocity. At the downstream boundary, the Neumann boundary condition was provided. The zero-gradient boundary condition was applied at all lateral boundaries. A homogeneous Neumann boundary condition was used for pressure at all these boundaries. The fruit fly body and wing surfaces were specified using high-density triangular surface mesh. Nonslip boundary conditions were applied on these surfaces. To achieve a periodic state of the flow field, the simulations were run for eight flapping cycles. The sufficient flapping cycles were adopted to ensure that the wake structures generated by flapping wings were fully affected by the outflow boundary condition.

To guarantee grid-independent simulation results, a grid refinement study was performed. Figure 3 shows the comparison of lift coefficient in three different grids densities. The results indicated that the differences between the medium grid (adopted in the current study) and fine grid were less than 2.1% for lift coefficient at their peaks.

The Reynolds number selected in this paper is 100, which is defined as $Re = U_\infty \bar{c}/\nu$, based on the incoming flow velocity (U_∞) and the mean wing chord ($\bar{c}$). The reduced frequency in the study is 0.65, which is defined as $k = f\bar{c}/U_\infty$. The values of these nondimensional parameters used here are consistent with real fruit flies in forward flight motion.[26]

In order to evaluate the aerodynamic performance, the surface pressure and shear stresses along the wing surfaces were obtained by solving the Navier–Stokes equations. The lift (F_L, along the vertical direction) and drag (F_D, along the horizontal direction) forces
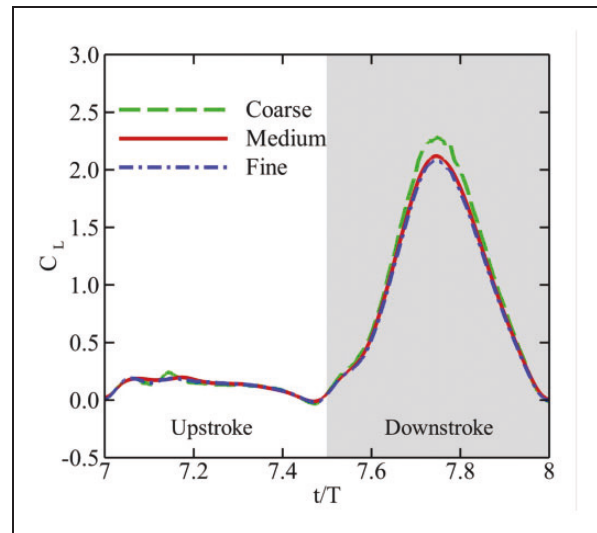

Figure 3. Comparison of lift coefficient of the wing for demonstrating the grid independence of the computed results. The grid employed in the simulations are $193 \times 129 \times 193 = 4.8 \times 10^6$ (for coars mesh), $289 \times 137 \times 249 = 9.9 \times 10^6$ (for medium mesh) and $353 \times 161 \times 321 = 18.2 \times 10^6$ (for fine mesh). The Reynolds number and reduced frequence for this case are 100 and 0.65, respectively.
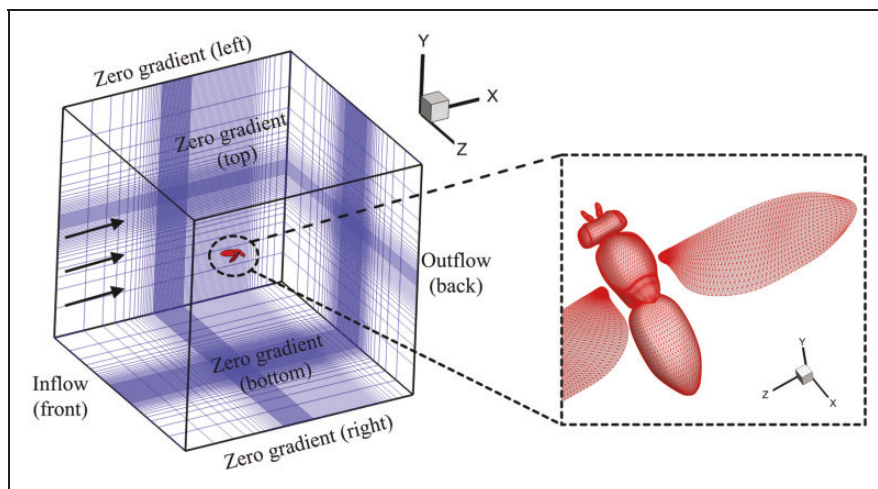

Figure 2. (a) Schematic of the computational mesh (approximately 10 million grids) and boundary conditions that were employed in the current simulations; (b) high-density surface mesh with approximately 29,000 and 5000 triangular elements were used to define the body and each wing, respectively.

are presented here as nondimensional coefficients, which are computed by $C_L = F_L/0.5\rho\bar{U}_{tip}^2 S$ and $C_D = F_D/0.5\rho\bar{U}_{tip}^2 S$, respectively. In which, C_L and C_D represent the lift and drag coefficients. Here, $\bar{U}_{tip}$ is the mean wing tip velocity, which is defined as $\bar{U}_{tip} = (1/T)_0^T\sqrt{u_{tip}^2 + v_{tip}^2 + w_{tip}^2}\,dt$, where u_{tip}, v_{tip}, and w_{tip} are wing tip velocity components in x, y, and z directions, respectively. Here, the S denotes the area of the wing surface. The normalized pressure involved in the current study was defined as $C_P = 2(p - p_\infty)/(\rho\bar{U}_{tip}^2)$.

The instantaneous aerodynamic power (P_{aero}) is the power needed to overcome air resistance and was calculated as the inner product of the velocity and the aerodynamic force. The way of computing the aerodynamic power followed the same definition as used in evaluating the aerodynamic power in cicada flight[11] and fruit fly flight.[36] The aerodynamic power coefficient was defined as $C_{PW} = P_{aero}/0.5\rho\bar{U}_{tip}^3 S$.

Evaluation of odor mass flux around antennae

The governing equation of odorant convection and diffusion in the air phase is given in equation (4)

$$\frac{\partial C'}{\partial t} = D\frac{\partial^2 C'}{\partial x_i \partial x_i} - u_i\frac{\partial C'}{\partial x_i} \tag{4}$$

where $i = 1, 2, 3$ indicates the component in the x-, y-, and z-directions; C' is the normalized odorant concentration defined by $C' = C/C_{in}$, in which C_{in} is the inlet or ambient air odorant concentration.

A pseudo-odor was uniformly and steadily released from the upstream inlet with a normalized concentration (C' at the inlet boundary equals 1). The Peclet number for the mass transfer is defined by $Pe = Re \cdot Sc$, where Sc reprsesents Schmidt number, which is the ratio between kinematic viscosity and mass diffusivity ($Sc = v/D$). Typical natural odor in the environment has a quite low diffusivity (D) in the air at normal temperature and pressure, ranging from 10^{-1} to 10^{-2} cm^2/s. So, the Sc has a range of 10^0 to 10^1. Based on the definition, the Peclet number in the current study is around 100. With the Peclet number in a range of 10^2–10^3, the convective odor transport dominants the system due to air movement, thus odor diffusion can be ignored in the present study.

By ignoring the odorant diffusion, the first term on the right-hand side of equation (4) is treated as zero. The odor mass flux through antenna is thus calculated by $C' \cdot \rho_{odor} \cdot U^*$, where ρ_{odor} is the density of odorant-laden air, and U^* represents the air velocity above the velocity boundary layer of antenna surface. The instantaneous profiles of U^* were obtained by using virtual probes placed above the boundary layer around the antenna. The thickness of the velocity boundary layer defined as the distance from the surface where the velocity reaches 99% of the freestream value. In addition, the density ratio between odorant-laden air and air is assumed as 1 ($\rho_{odor} = \rho_{air} = 1.225\,\text{kg m}^{-3}$). The normalized odor intensity (J_{odor}) was used here to estimate the capability of olfactory detection, which is defined as $J_{odor} = \rho_{odor}U^*/\rho_{air}U_\infty$. The numerator ($\rho_{odor}U^*$) represents the odor mass flux around the antenna. The higher value of odor intensity (J_{odor}) represents a better olfactory sensitivity during flight.

To visualize the odor plume structures, the Lagrangian tracking approach was applied by assuming that odor transport is dominated by the convective flow field. Computational neutral-buoyant particle tracers have been widely used to mimic the smoke[37] and bubble[38] with good experimental agreement, when diffusion is low. The time step of the tracking proses is set as 0.001. As illustrated in Figure 4, pseudo-odor path undergoes a translation downstream before reaching the flapping wings due to the uniform velocity field.

Results and discussion

In this section, the aerodynamic performance and olfactory sensitivity were evaluated for a fruit fly model in upwind surge with different wing pitch kinematics. The vortex structures around insect wing and body are presented in detail. The odor plume structure disturbed by flapping wings were then visualized using the Lagrangian tracking approach to reveal its underlying flow physics.
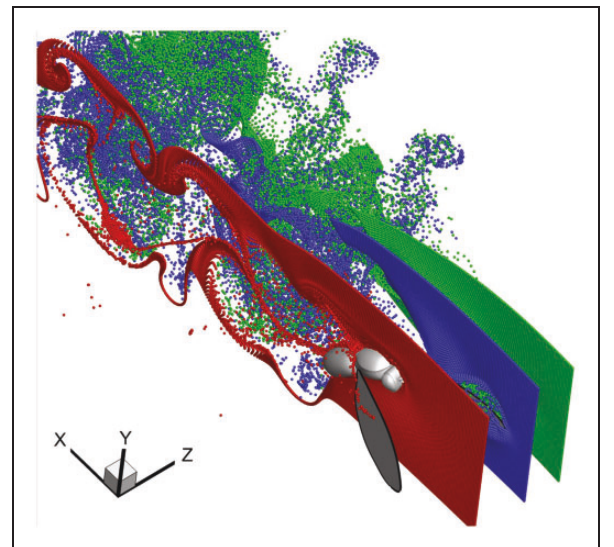

Figure 4. An illustration of passive odor tracers released in upstream. Red, blue, and green colors represent three different releasing locations at mid-body plane, mid-wingspan, and wingtip, respectively.

Aerodynamic performance and olfaction sensitivity

To ensure both aerodynamic and olfactory functions reached a periodic state, eight flapping cycles were performed in all simulations. Figure 5 presents the aerodynamic performance and olfactory sensitivity results during the last two flapping cycles. Similar to previous studies of forward flying insects[10,12] the majority of lift was produced during the downstroke, and the force peaks appeared during the mid-downstroke (see Figure 5(a)). As shown in Figure 5(b), the average value of drag coefficients for all cases was close to zero, which indicated the force balance was almost achieved along the horizontal direction. Thus, the fruit fly was close to a self-propelled upwind surge with a constant flying speed. Most aerodynamic power was consumed during the downstroke (Figure 5(c)), and its peak value appeared during the mid-downstroke. Due to the effects of wing–wing interaction, secondary peaks for forces and power coefficients occurred during the wing reversal phases, especially for the wing pitch kinematics with $C = 3$. Unlike the force and power profiles, odor intensity peak occurred during the wing reversal (supination period in Figure 5(d)). As the wing pitch kinematics

changed to a step-function profile ($C = 3$), the odor intensity gradually raised during the pronation period as well. The average aerodynamic performances and odor intensity for all the cycles obtained from the simulations are summarized in Table 1. The data show that as the wing kinematics profiles changed from a sinusoidal function ($C = 0$) to a step function ($C = 3$), the lift generation decreased by approximately 14%, while the odor intensity around olfactory surface enhanced by about 10%. The wing pitch kinematics profile with $C = 2$ achieves the optimal aerodynamic efficiency, in terms of lift-to-power

Table 1. Cycle-averaged lift coefficient ($\bar{C}_L$), aerodynamic power coefficient ($\bar{C}_{PW}$), lift-to-power ratio ($\bar{C}_L/\bar{C}_{PW}$), and odor intensity ($\bar{J}_{odor}$) with different wing pitch kinematics.

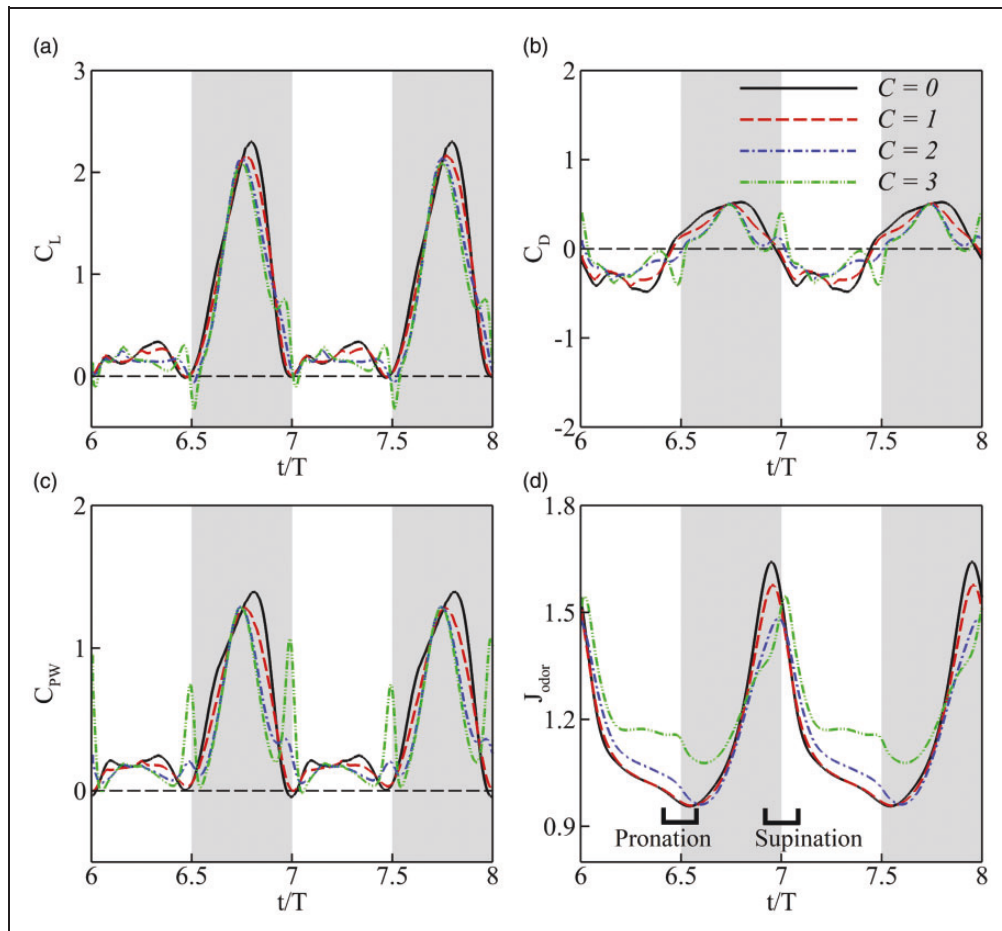|	$\bar{C}_L$	$\bar{C}_{PW}$	$\bar{C}_L/\bar{C}_{PW}$	$\bar{J}_{odor}$
$C = 0$	0.674	0.467	1.444	1.155
$C = 1$	0.642	0.415	1.548	1.144
$C = 2$	0.593	0.378	1.571	1.148
$C = 3$	0.578	0.409	1.412	1.270

Figure 5. Time evolution of lift coefficient (a), drag coefficient (b), aerodynamic power coefficient (c), and normalized odor intensity (d), when the flapping wing underwent different wing pitch kinematics by adjusting the *C* factor in equation (2). The grey shaded region indicates the downstroke.
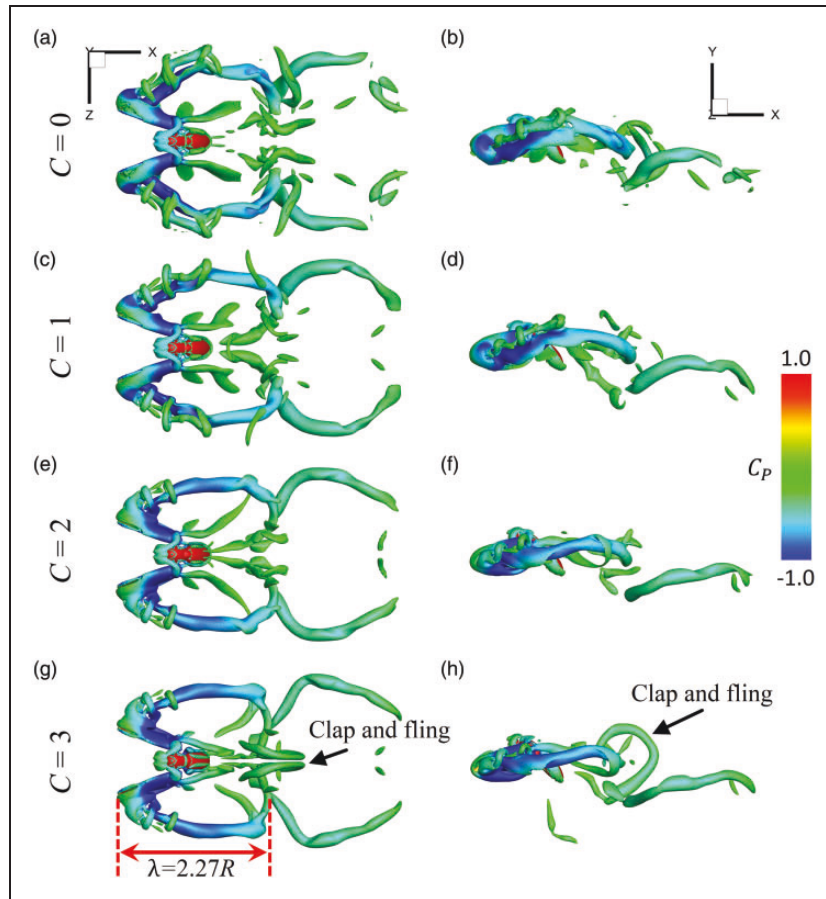
Figure 6. Comparison of wake structures for the wing pitch kinematics with $C = 0$ (a–b), $C = 1$ (c–d), $C = 2$ (e–f), and $C = 3$ (g–h). The wake structures were visualized by Q-criterion and color coded using normalized pressure. The streamwise wakelength (λ) of the downstroke vortex structures was quantified in terms of wing length (R). The vortex structure that was generated due to the clap-and-fling is labeled in plots (g–h).
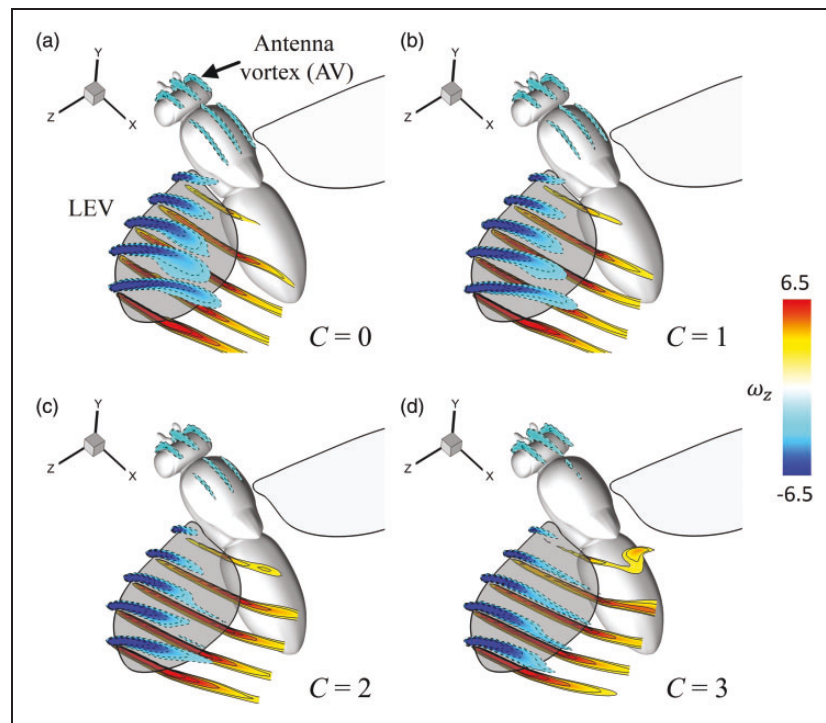

Figure 7. Comparison of leading-edge vortex (LEV) and antenna vortex (AV) formation when the wing flaps around the middle of downstroke with different wing pitch kinematics.

ratio ($\bar{C}_L/\bar{C}_{PW}$). However, the overall trend of the odor intensity ($\bar{J}_{odor}$) is quite different from the aerodynamic performance. The minimal value of odor intensity appears with $C = 1$. As the C factor continuously increases, the value of odor intensity reaches an increasingly higher value. This different changing trends between the aerodynamic performance and olfactory sensitivity indicate that the flapping wings benefit each function based on different mechanisms. There may exist a conflict of interest between both functions. By tailoring the C factor in the hyperbolic function, the aerodynamic performance could increase, while it would sacrifice the odor intensity received by the olfactory receptors (i.e. antenna). It is possible that the insect might have to achieve a
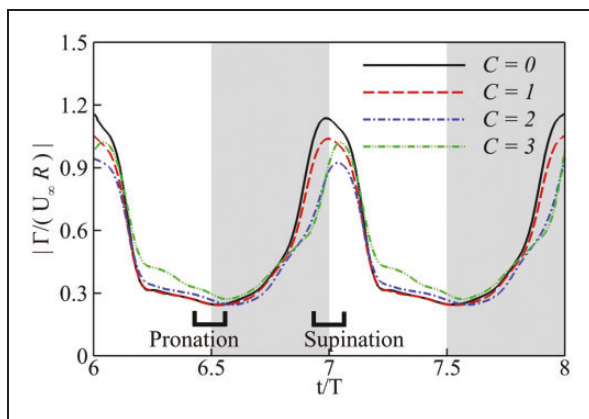

Figure 8. Time evolution of the normalized vortex circulation around antenna for different wing pitch kinematics. The vortex circulation was nondimensionalized using incoming flow velocity (U_∞) and wing length (R).

balance between two functions, instead of purely optimizing either one of them.

Figure 6 shows the wake topology generated by different wing pitch kinematics, and they are visualized using Q-criterion and color coded by the normalized pressure. In general, the wake is dominated by a chain of vortex loops behind the wing and periodically shed at the wing reversal in each flapping cycle. The streamwise wakelength (λ) of the downstroke vortex structure is around $2.37R$, where R is the wing span length. It is not surprising that with a step-function like wing pitch kinematics profile ($C = 3$), the interaction between the flapping wing pair is significantly enhanced during the pronation phase, which is also known as clap-and-fling.[39] The vortex structure that is generated due to the clap-and-fling is labeled in Figure 6(g) and (h).

Next, the LEV around insect wing and antenna vortex (AV) that were developed around insect head are compared with various wing pitch kinematics, as shown in Figure 7. For each case, multiple 2D slides cuts were taken along the insect's wing and body. The size of the LEV continues to grow proportionally along the span. As the wing pitch profiles change from $C = 0$ to $C = 3$, the size of LEV decreases, while shows better LEV attachment. In addition, the flapping wings induce strong air flow over its body and form an antenna vortex around its head.

To quantify the strength of the AV, the z-direction vorticity field (ω_z) was visualized using contour lines. After each vortex was manually identified, a closed contour line was generated around this vortex with a specified level, and the circulation (Γ) was then
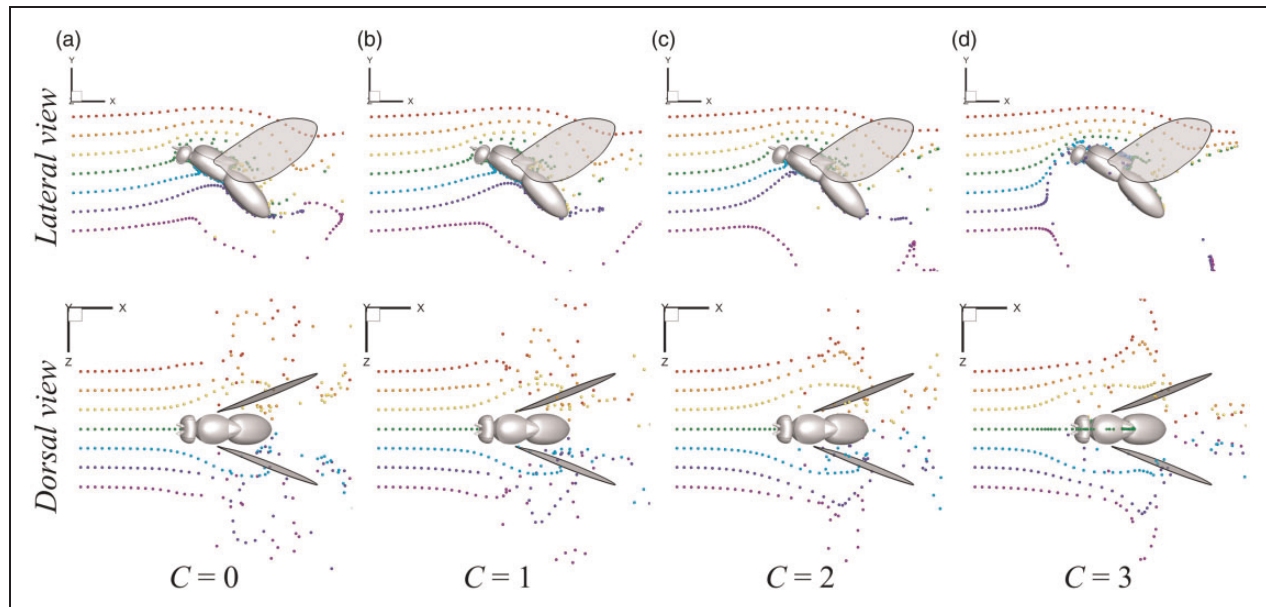

Figure 9. Odor plume structure was visualized using neutral-buoyant particles released from lateral (the first row) and dorsal (the second row) locations, respectively: (a) $C = 0$, (b) $C = 1$, (c) $C = 2$, (d) $C = 3$. The snapshots were selected at the time points of peak odor mass flux to the antenna. The colors of the particles indicate different release locations.

calculated by integrating the z-direction vorticity along this line, and then normalized by $U_\infty \cdot R$. Although the magnitude of the circulation depends on the chosen contour level, the characteristic behavior of the vortex is not affected by this choice. As illustrated in Figure 8, the strength of vortex circulation above the antenna synchronizes with the flapping motion and presents peak values during the supination phase. By comparing Figure 8 with Figure 5(d), the general changing trend of antenna vortex circulation is similar to the odor intensity. This observation indicates that the flapping wings enhance the odor intensity by inducing stronger airflow above its head during the supination phase and thus enhance the olfactory function in odor-tracking flight.

Smart wing rotation in odor-tracking flight

The odor sampling range induced by flapping wings was visualized by parallel releasing streams of pseudo odor plume uniformly in upstream, as shown in Figure 9. The colors of the particles indicate different releasing locations. For the sinusoidal function ($C = 0$), only the green particles were able to pass through the antenna region induced by the flapping motion. By changing the wing pitch kinematics to the step function ($C = 3$), the wing could draw more particles to pass through the olfactory region (i.e. the cyan and blue particles). The spatial sampling ranges of odor also increased in the vertical direction, which implied a better olfaction detection (the first row of Figure 9). However, if the odor particles were released from the top view, surprisingly, only
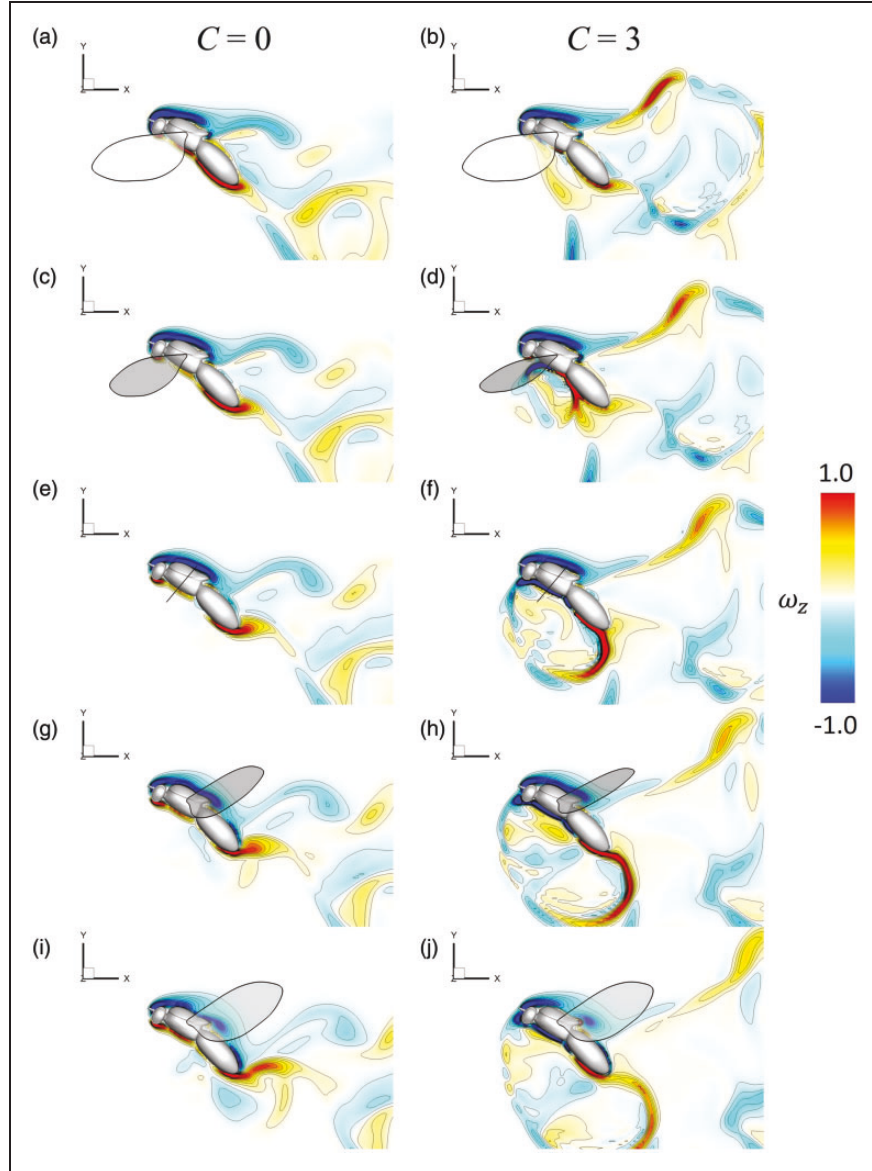

Figure 10. Comparison of the vortex structure between $C = 0$ (the left column) and $C = 3$ (the right column) during the upstroke at $t/T = 7.0$ (a–b), 7.125 (c–d), 7.25 (e–f), 7.325 (g–h), 7.5 (i–j). The slide cut is taken around the body center. The z-direction vorticity is normalized by multiplying the wing length (R) and dividing it by the incoming flow velocity (U_∞).

the center of the particle was able to pass through the antenna region. This observation is applicable to all different wing pitch kinematics. Although the vertical odorant sampling range of insect can be significantly amplified by the flapping motion, the flapping wings cannot transport odor laterally. It is speculated that this fluid mechanism for the odor transport might be the reason why insect needs to present zigzagging cross-wind motion during the odor-guided navigation. Based on the present CFD simulation results, the lateral component of flow speed near the olfactory receptors (i.e. antenna) is canceled out due to the symmetrical flapping motion between the left and right wings. The asymmetrical flapping motion during a zigzagging cross-wind motion can potentially enhance the lateral component of airflow induced by the flapping wings. The horizontally oriented antenna in many insects together with the zigzagging motion may supplement the sampling range in the horizontal direction during the odor-guided navigation. Of course, this hypothesis needs to be tested in future investigations.

Figure 10 compares the vortex structures around the center of insect body between the sinusoidal function ($C = 0$) and the step function ($C = 3$) wing pitch kinematics. The fast wing rotation during the wing reversal phase created a wake region under the insect body for the case with $C = 3$. This wake region was created when the wing pair interacted with each other during the supination phase. This can explain why more pseudo odor plume particles can be flicked upward to the insect antenna in Figure 9(d) (top panel). It has been widely realized that the clap and fling mechanism during the pronation phase can enhance the force generation.[40–43] However, few studies have focused on the contribution of supination phase of flapping wings. The current study suggested that the wing–wing interaction during the supination phase may not be important in terms of aerodynamic performance, but it could potentially enhance the olfactory sensitivity by amplifying the vertical sampling range of odor-tracking flight.

In addition, it was observed that the odor sampling enhanced by flapping wings consisted of two stages of accumulation. During the downstroke (Figure 11(a)), the downward flapping wings push airflow towards its body and attract some of the stream particles around the antenna region, but they have the limitation to induce the particles far from its body. Once the wing starts to reverse and flap upward (Figure 11(b)), the trailing-edge close to the wing root rotates quickly and kicks surrounding airflow upward, and thus brings these distant particles to the antenna. This phenomenon is especially evident for a step-function such as wing pitch kinematics ($C = 3$ in Figure 9(d), top row).
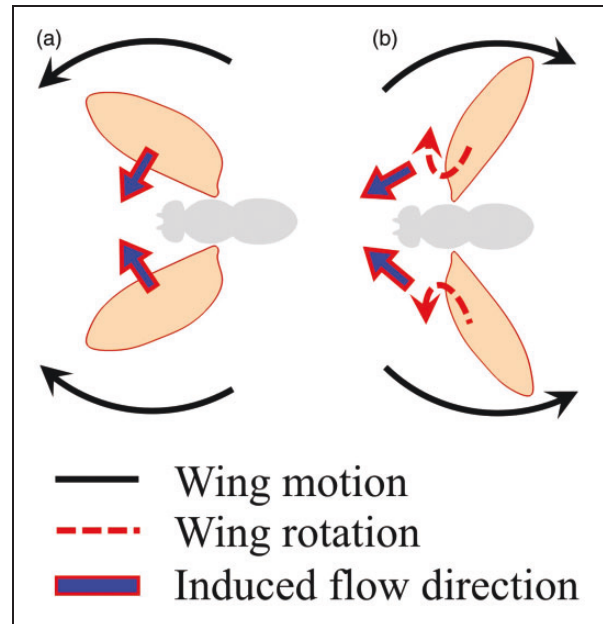

Figure 11. Schematics of the odor trapping (a) and flicking (b) mechanism that enhances the olfaction sensitivity in an odor-tracking flight.

Conclusions

In this study, the effects of wing pitch kinematics on the aerodynamic and olfactory functions were numerically investigated for a fruit fly model in an upwind surge. Using a high-fidelity immersed-boundary-method-based CFD solver, the author carried out the unsteady flow simulations of the wing pitch profiles, varying from a sinusoidal function to a step function. The aim of this study was to examine how the flapping motion affects both aerodynamic performance and olfactory sensitivity. The simulation results revealed that the changing of wing pitch kinematics could modify the wing–wing interaction during the wing reversal phases. During the pronation phase, the flapping wings interacted with each other, created distinct vortex, and enhanced its associated force generation, which is also well known as clip-and-fling mechanism. During the supination phase, the flapping wings trapped the odor plumes and then flicked them upward to the olfactory receptors (i.e. antenna). Through this trap-and-flick mechanism, the olfactory sensitivity could be enhanced by up to 10%. However, the enhancement of olfactory sensitivity was achieved at a cost. It decreased the lift generation by around 14%. In other words, there is always a trade-off between the aerodynamic and olfactory functions. In order to maintain both aerodynamic and olfactory functions, it is speculated that the natural flyers may sacrifice certain aerodynamic or olfactory potential to achieve a balance between both functions. It is expected that the current study would offer some general insights into the flow physics of odor-guided navigation in nature.

ORCID iD

Chengyu Li https://orcid.org/0000-0002-8379-2423

References

1. Ellington CP, vandenBerg C, Willmott AP, et al. Leading-edge vortices in insect flight. *Nature* 1996; 384: 626–630.
2. Dickinson MH, Lehmann FO and Sane SP. Wing rotation and the aerodynamic basis of insect flight. *Science* 1999; 284: 1954–1960.
3. Young J, Walker SM, Bomphrey RJ, et al. Details of insect wing design and deformation enhance aerodynamic function and flight efficiency. *Science* 2009; 325: 1549–1552.
4. Bomphrey RJ, Nakata T, Phillips N, et al. Smart wing rotation and trailing-edge vortices enable high frequency mosquito flight. *Nature* 2017; 544: 92.
5. Dong H, Bode-Oke AT and Li C. Learning from nature: unsteady flow physics in bioinspired flapping flight. In: *Flight physics-models, techniques and technologies*. London: InTech, 2018.
6. Sane SP and Jacobson NP. Induced airflow in flying insects II. Measurement of induced flow. *J Exp Biol* 2006; 209: 43–56.
7. Loudon C and Koehl M. Sniffing by a silkworm moth: wing fanning enhances air penetration through and pheromone interception by antennae. *J Exp Biol* 2000; 203: 2977–2990.
8. Li C, Dong H and Zhao K. A balance between aerodynamic and olfactory performance during flight in Drosophila. *Nat Commun* 2018; 9: 3215.
9. van den Berg C and Ellington CP. The vortex wake of a 'hovering' model hawkmoth. *Philos T Roy Soc B* 1997; 352: 317–328.
10. Sun M and Wu JH. Aerodynamic force generation and power requirements in forward flight in a fruit fly with modeled wing motion. *J Exp Biol* 2003; 206: 3065–3083.
11. Wan H, Dong H and Gai K. Computational investigation of cicada aerodynamics in forward flight. *J R Soc Interface* 2015; 12: 20141116.
12. Liu G, Dong H and Li C. Vortex dynamics and new lift enhancement mechanism of wing–body interaction in insect forward flight. *J Fluid Mech* 2016; 795: 634–651.
13. Liang B and Sun M. Aerodynamic interactions between wing and body of a model insect in forward flight and maneuvers. *J Bionic Eng* 2013; 10: 19–27.
14. Wang J, Ren Y, Li C, et al. Computational investigation of wing-body interaction and its lift enhancement effect in hummingbird forward flight. *Bioinspir Biomim* 2019; 14: 046010.
15. Justus KA, Schofield SW, Murlis J, et al. Flight behaviour of Cadra cautella males in rapidly pulsed pheromone plumes. *Physiol Entomol* 2002; 27: 58–66.
16. van Breugel F and Dickinson MH. Plume-tracking behavior of flying Drosophila emerges from a set of distinct sensory-motor reflexes. *Curr Biol* 2014; 24: 274–286.
17. Vickers NJ. Winging it: moth flight behavior and responses of olfactory neurons are shaped by pheromone plume dynamics. *Chem Senses* 2005; 31: 155–166.
18. Liu H and Aono H. Size effects on insect hovering aerodynamics: an integrated computational study. *Bioinspir Biomim* 2009; 4: 15002.
19. Li C and Dong H. Wing kinematics measurement and aerodynamics of a dragonfly in turning flight. *Bioinspir Biomim* 2017; 12: 026001.
20. Li C, Wang J and Dong H. Proper orthogonal decomposition analysis of flapping hovering wings. *AIAA Paper 2017-0327*, 2017.
21. Xu M, Wei M, Li C, et al. Adjoint-based optimization for thrust performance of three-dimensional pitching–rolling plate. *AIAA J* 2019; 57: 3716–3727.
22. Warren TL, Giraldo YM and Dickinson MH. Celestial navigation in Drosophila. *J Exp Biol* 2019; 222: jeb186148.
23. Fry SN, Sayaman R and Dickinson MH. The aerodynamics of free-flight maneuvers in Drosophila. *Science* 2003; 300: 495–498.
24. Bergou AJ, Ristroph L, Guckenheimer J, et al. Fruit flies modulate passive wing pitching to generate in-flight turns. *Phys Rev Lett* 2010; 104: 148101.
25. Li C, Wang J, Liu G, et al. Passive pitching mechanism of three-dimensional flapping wings in hovering flight. In: *Proceedings of the ASME-JSME-KSME 2019 8th joint fluids engineering conference*, San Francisco, CA, USA, 2019.
26. Meng X and Sun M. Wing kinematics, aerodynamic forces and vortex-wake structures in fruit-flies in forward flight. *J Bionic Eng* 2016; 13: 478–490.
27. Berman GJ and Wang ZJ. Energy-minimizing kinematics in hovering insect flight. *J Fluid Mech* 2007; 582: 153–168.
28. Li C, Dong H and Cheng B. Effects of aspect ratio and angle of attack on tip vortex structures and aerodynamic performance for rotating flat plates. AIAA 2017-3645, 2017.
29. Wang J, Li C, Zhu R, et al. Wake structure and aerodynamic performance of passively pitching revolving plates. AIAA 2019-1376, 2019.
30. Li C and Dong H. Wake structure and aerodynamic performance of low aspect-ratio revolving plates at low Reynolds number. AIAA Paper 2014-1453, 2014.
31. Li C and Dong H. Three-dimensional wake topology and propulsive performance of low-aspect-ratio pitching-rolling plates. *Phys Fluids* 2016; 28: 071901.
32. Li C, Dong H and Liu G. Effects of a dynamic trailing-edge flap on the aerodynamic performance and flow

structures in hovering flight. *J Fluid Struct* 2015; 58: 49–65.

33. Wang J, Li C, Ren Y, et al. Effects of surface morphing on the wake structure and performance of flapping plates. AIAA 2017-3643, 2017.

34. Li C and Dong H. Quantification and analysis of propulsive wake topologies in finite aspect-ratio pitching-rolling plates. AIAA Paper 2016-4339, 2016.

35. Li C, Jiang J, Dong H, et al. Computational modeling and validation of human nasal airflow under various breathing conditions. *J Biomech* 2017; 64: 59–68.

36. Aono H, Liang F and Liu H. Near- and far-field aerodynamics in insect hovering flight: an integrated computational study. *J Exp Biol* 2008; 211: 239–257.

37. Yokoyama N, Senda K, Iima M, et al. Aerodynamic forces and vortical structures in flapping butterfly's forward flight. *Phys Fluids* 2013; 25: 021902.

38. Harbig RR, Sheridan J and Thompson MC. Reynolds number and aspect ratio effects on the leading-edge vortex for rotating insect wing planforms. *J Fluid Mech* 2013; 717: 166–192.

39. Lehmann FO, Sane SP and Dickinson M. The aerodynamic effects of wing-wing interaction in flapping insect wings. *J Exp Biol* 2005; 208: 3075–3092.

40. Cooter R and Baker P. Weis-Fogh clap and fling mechanism in Locusta. *Nature* 1977; 269: 53–54.

41. Miller LA and Peskin CS. A computational fluid dynamics of 'clap and fling' in the smallest insects. *J Exp Biol* 2005; 208: 195–212.

42. Miller LA and Peskin CS. Flexible clap and fling in tiny insect flight. *J Exp Biol* 2009; 212: 3076–3090.

43. Bennett L. Clap and fling aerodynamics-an experimental evaluation. *J Exp Biol* 1977; 69: 261–272.